EXPERIMENTAL AND THEORETICAL RESEARCH OF THE j x B ACCELERATION OF THE SHOCK-INDUCED FLOW IN ARGON

SHIBATA, Kohki
Department of Aeronautical Engineering, Kyushu University : Postgraduate Student

IWASAKI, Matsunosuke
Department of Aeronautical Engineering, Kyushu University : Professor

https://doi.org/10.5109/7172197

出版情報：Reports of Research Institute for Applied Mechanics. 19 (64), pp.237-264, 1972. 九州大学応用力学研究所

Reports of Research Institute for Applied Mechanics
Vol. XIX, No. 64, 1972

EXPERIMENTAL AND THEORETICAL RESEARCH OF THE $j \times B$ ACCELERATION OF THE SHOCK-INDUCED FLOW IN ARGON*

By Kohki SHIBATA** and Matsunosuke IWASAKI***

The problem of the acceleration of the shock-induced flow under $j \times B$ force was investigated experimentally and theoretically for the case when the axial plasma length behind the shock front was considerably short compared with the accelerator length and the flow was essentially unsteady. The behavior of the luminous plasma was observed mainly with an ultra-high-speed camera, the photographs of which show that partial protrusions of the shock front grew near the electrodes in our accelerator with a circular cross-section. Experiments were performed for several combinations of current density j and magnetic flux density B. The quantitative measurements of the shock velocity change were compared with the theoretical results which were obtained by characteristic calculations considering the shock front and the contact surface boundary conditions. Two flow models, frozen and equilibrium, were adopted in these calculations to estimate mainly the influence of the Joule heating effect on the shock acceleration.

1. Introduction

The electro-magnetic acceleration of the shock-induced flow has been studied by several researchers and many important basic informations have been obtained.

Hogan[1] and Leonard[2] reported experimental investigations of the increase of shock velocity and particle velocity and the momentum and energy balance between the electro-magnetic energy and the flow energy, etc. The main purpose of their investigations lies in the determination of the flow velocity increase obtainable from a given amount of $j \times B$ force. It seems to us that their investigations lead to the problem about the existence and the nature of the loss mechanisms which is basic in plasma acceleration.

Hogan treated the flow between the shock and the contact surface as a

* Read at the IUTAM Symposium on Dynamics of Ionized Gases, Sept. 17, 1971, at Tokyo.
** Postgraduate Student, Department of Aeronautical Engineering, Kyushu University, Fukuoka, Japan.
*** Professor, Department of Aeronautical Engineering, Member of Research Institute for Applied Mechanics (part-time staff), Kyushu University, Fukuoka, Japan.

slug of constant mass. This considerably simplifies the unsteady flow problem, since the slug length is short compared with the accelerator length. On the other hand, Leonard treated the shock-heated region as a quasi-steady flow by making the duration of the flow comparatively long.

We think that if we want to clarify more basic problems of the electro-magnetic acceleration such as the nature of the loss mechanism, it seems to be necessary to study the acceleration process itself in more detail using as few simplifying assumptions as possible. From this point of view, the authors studied the acceleration of the shock-heated flow under the electro-magnetic field both experimentally and theoretically.

There are several theoretical studies of this interaction problem. For example, Rosciszewski[2] proposed a useful characteristic rule which was obtained by assuming that the shock-heated region extended infinitely downstream without any discontinuity behind the shock front. Also Mirels[4] treated the interaction of the piston driven shock tube flow with transverse magnetic field using a linearized theory based on a small perturbation assumption.

Although their results are useful, it is rather difficult to apply their simplified models directly to the actual acceleration process. To overcome these difficulties, and also to obtain the flow picture at the same time, we tried to calculate the flow field in the shock-heated region by the method of characteristics.

Corresponding to this theoretical approach, we tried to observe the shock acceleration process and the flow behavior experimentally by using a transparent glass tube accelerator and observing the behavior of the luminous shock-heated region with an ultra-high-speed camera.

Although we tried to make as few simplifying assumptions as possible in the experimental and theoretical treatment, there still remain several uncertainties, since, for example, the acclerator cross-section is circular, the current density inside the plasma is indirectly calculated from the total current based on a certain assumption instead of measuring its distribution directly, and the flow field is assumed to be quasi-one-dimensional. Thus the results obtained in the present research are not yet complete and leave many problems to the future. Still we hope that they supply some useful facts about the shock acceleration phenomena.

2. Experimental Apparatus and the Method of Measurement

The idealized physical model of the acceleration phenomena treated in this investigation can be described as in Fig. 1. The accelerator consists of a set of magnetic coils that produces uniform magnetic field B in the y-direction and a pair of electrodes that produces electric field normal to the magnetic field and the flow direction. These orthogonal fields generate $j\times B$ force, i. e. Lorentz force, in the axial x-direction in the plasma between the electrodes. The problem treated here is the acceleration process of the shock-induced plasma inside this accelerator, in other words, the observation of the accelera-

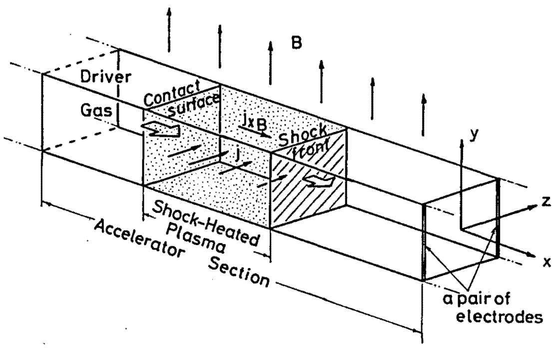

Fig. 1 Physical model

tion and the behavior of the shock wave and the flow behind it. The experimental apparatus was designed to closerly realize this ideal situation. Its schematic diagram is shown in Fig. 2. Some descriptions of the apparatus and the method of measurement will be given below.

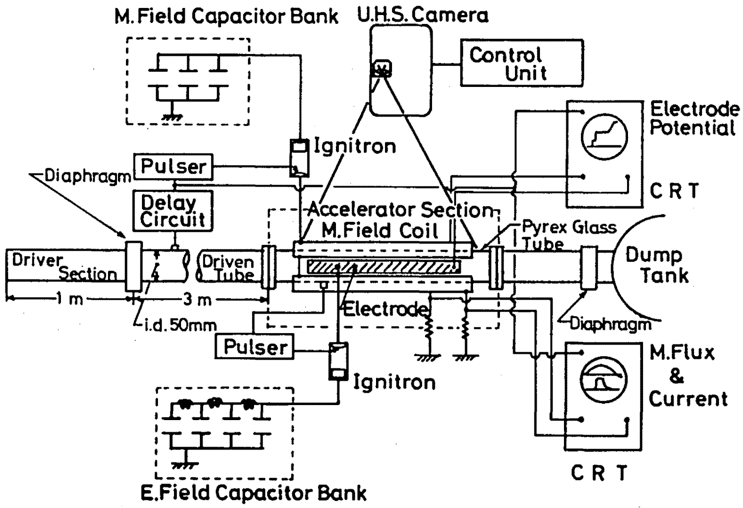

Fig. 2 Schematic diagram of the experimental apparatus.

2. 1. Shock tube

The combustion-driven shock tube used in this experiment had an inside diameter of 50 mm and consisted of a driver section which was 1 meter long and fabricated with chromium steel of 25 mm thickness, a driven section about 4.5 meters long including the accelerator, and a dump tank. The accelerator was placed about 3 meters downstream of the diaphragm. The dump tank was separated from the driven section by a cellophane diaphragm.

The driver gas was stoichiometric mixture of hydrogen and oxygen with 70 % helium as a diluent. To produce uniform combustion, four spark plugs were mounted flush with the inner surface in a spiral arrangement along the driver tube. The working gas in the driven section was argon with initial pressure p_1 of either 1 mmHg or 2 mmHg. To obtain highest possible purity, the driven section was first evacuated to the limit of the vacuum system, which was 0.03 to 0.05 mmHg, then it was washed with 1 atm argon three to four times before it was evacuated to the planned initial pressure.

Two aluminium plates each with 0.8 mm thickness were used as the diaphragm to sepatate the driven section from the driver section. To permit the diaphragm to open into petals, two grooves were cut at right angles to each other.

The spark plugs were fired by four ignition coils, whose primary coils were driven by a discharge from a capacitor charged to 400 volts. Its discharge was controlled by a silicon controled rectifier (SCR) triggered by the central control system via a photo-electronic relay circuit. This photo-relay was necessary to decouple the shock tube from other electronic systems.

2. 2. Accelerator section

The accelerator was constructed with 1 meter long Pyrex glass pipe with 53 mm inside diameter and 5 mm thickness. Two 50 cm long copper strip electrodes with 0.3 mm thickness were bonded on the inner surface, subtending an angle of 60 degrees in the circumferential direction. Each of the electrodes was connected with the external electrical source with three leads, which also acted as structural supports. The leading edge of the electrode was 20 cm downstream of the front end of the glass pipe. A shock detector ion probe placed 7 cm downstream of the front end of the electrode served as a trigger for the pulser circuit shown in Fig. 2, which discharged the capacitor bank for the electric field application.

Although it was desirable to reinforce the glass pipe against the inner pressure of the flow and the electro-magnetic force, only a small portion near the leads from the electrodes was reinforced with fiberglass reinforced plastics (FRP) to retain the accelerator as transparent as possible to enable large portion of the shock-heated region to be photographed with the ultra-high-speed camera.

The transverse magnetic field was generated by two air-cored coils with total 84 turns. They were first wound in rectangular shapes, then bent to saddle shapes, and mounted on both sides of the accelerarator tube using wooden retainer framer, which served both to prevent the deformation of the coils by the electro-magnetic force and to keep the proper distance between the coils and the accelerator tube. Ordinary vinyl-coated electric wire with 3 mm outside diameter for maximum 600-volt use was used to fabricate the coils, which was sufficient for our purpose, because the high voltage and large current used in this experiment lasted only for a very short time.

2. 3. Electrical systems

Since the current supplied to the electrodes must have a wave form which was as near a step function as possible, it was supplied by a lumped parameter transmission-line capacitor bank with four sections, each of which had a 160 μ F capacitor bank with the working voltage of 5 kV and a few μ H inductor.

The current form did not change when it was discharged through the plasma, since impedance of the plasma between the electrodes was sufficiently small compared with the lead line impedance. The maximum current obtained from this system was about 24,000 A. A typical wave form is shown in Photo 1.

The discharge from the capacitor bank was switched by a Mitsubishi ignitron MI-3100C with a maximum hold-off voltage of 7.5 kV. Since the delay time of this switching system was only 1 to 2 μ sec, the electric current could be supplied almost instantly after the shock arrived at the ion detector probe.

The current for the magnetic field was supplied by a 26.6 μ F capacitor bank with 30 kV working voltage, and was also switched by an ignitron and a pulser circuit shown in Fig. 2.

Since the circuit was designed to ring with a half-cycle time of about 800 μ sec, the magnetic field strength could be considered almost constant during the duration of the observed phenomenon, which was less than 100 μ sec, if its peak could be made to coincide with the shock arrival. To achieve this, the shock arrival was detected about 3 m upstream of the accelerator, and its signal, delayed by an appropriate amount, was used to trigger the pulser circuit.

A typical discharge wave form is shown in Photo 2. The maximum charge voltage was limited by the structural strength of the coils to 19 kV, which generated a magnetic flux density of about 8,500 Gauss.

2. 4. Measuring instrumentation

The shock wave acceleration and the flow behavior inside the accelerator were observed with an ultra-high-speed camera and a streak camera. The former was used to record the time-to-time shock position enabling quantitative determination of the shock behavior, while the latter was used for supplementary purpose.

The ultra-high-speed camera was a Nikon-Uemura UHF500B camera, which could take 400 pictures at a maximum framing speed of 500,000 frames per second. The exposure time at this speed was 0.2 μ sec and during this time shock front traveled about 1 mm.

The most important component of this camera was rotating mirror driven by a high-speed nitrogen turbine. As the maximum operating time of this turbine was limited to within one minute, a special synchronization procedure was necessary to make the firing and the measurement at a precise time when the turbine reached the planned framing speed. Fortunately this camera had a solenoid driven shutter system with a flash light contact switch, which operated when the turbine speed reached a preset value. The signal from this flash liglt switch was used to trigger the synchronization system. When this system is triggered, it first indicates the time for the operators of the cathode-ray tubes (CRTs) to actuate the recording cameras of the CRTs. And then, only after all the cameras have been actuated, the system fires the shock tube and at the same time triggers the digital counter for instantaneous framing speed monitoring. When the shutter of the ultra-high-speed camera is closed after one second, the turbine gas flow is automatically cut off, even when the shock tube has not been fired by some miscoordination, thus preventing the turbine from exceeding the speed limit.

As stated above, the exact framing speed of the camera was measured by counting the pulse signal from the turbine over 0.1 sec interval starting from the instant of the shock tube ignition.

Since the shock front reaches the accelerator section within several milliseconds from the ignition, this record was assumed to represent the framing speed of the camera during the acceleration phenomenon. To check this, several firings were made without accelerative force fields and the shock speed was determined by measuring the time interval between the pulse signals from two ion probes. This result was compared with the shock speed calculated from the simultaneous photographic record using the above mentioned framing speed measurement. Both agreed within about 3 % with each other, which was within the inherent errors of the measuring instruments.

The magnetic flux density was measured in an indirect way, as it was almost impossible to measure it during the actual firing when the coils were mounted on both sides of the tube. Before they were mounted, the magnetic flux density was measured using a search coil by recording the electronically integrated value of its output on a CRT. The value of the current through the coils were recorded at the same time, and the magnetic flux density during the actual firings were determined by comparing this with similar CRT records of the current value duing the actual runs.

Also the spatial distribution of the magnetic flux density was measured. This measurement showed that the density uniformity was practically satisfactory, since the nature of this experiment does not require very high uniformity.

The current for the electric field application was determined by measuring the potential drop across a noninductive shunt resistor using a differential amplifier. The accuracy of this method was checked by supplementary measurements using a Rogowski coil.

The electric potential difference between the electrodes was similarly measured using a differential amplifier after dividing its value to one fifth using a series of resistors.

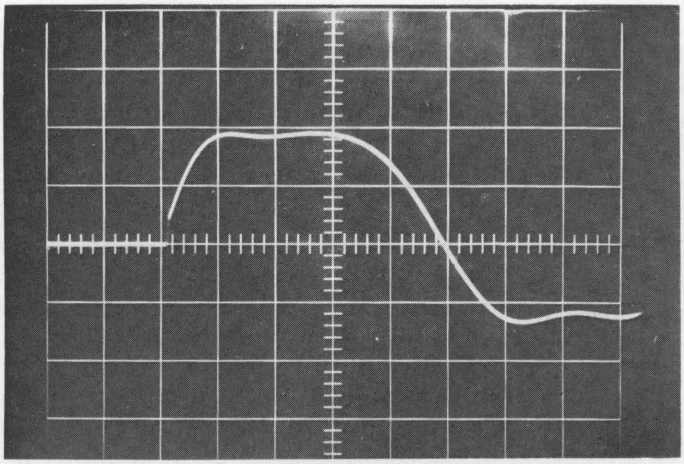

Photo 1 Typical record of the discharge current. (50 μ sec/div.)

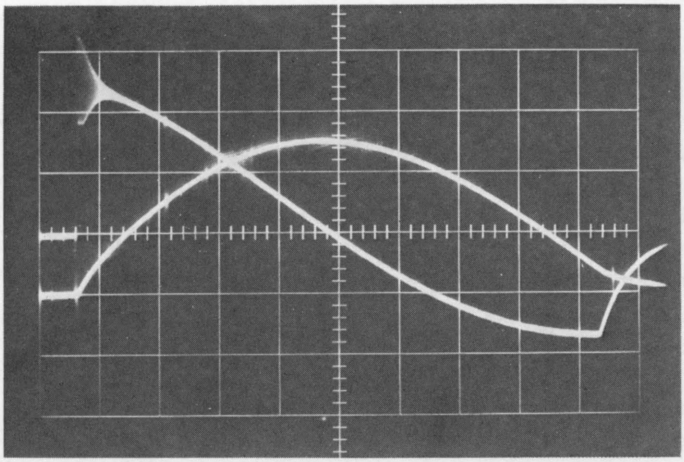

Photo 2 Typical record of the magnetic flux density (100 μ sec/div.)
Upper; Signal of search coil
Lower; Integrated wave form of the above signal

(Facing p. 242)

3. Experimental Results

3. 1. Preliminary observations

Prior to the acceleration experiments, basic conditions of the flow field in the accelerator section were observed without applying the magnetic and electric fields. Since the high temperature of the shock-heated plasma estimated to be about 12,000°K made it highly luminous, the flow field could be observed directly by an ultra-high-speed camera or a streak camera.

The length of the plasma from the shock to the contact surface obtained with our shock tube was rather short, and, though changed more or less according to the test conditions, was about 10 cm when p_1 was from 1 to 2 mmHg. Also it was still gradually increasing at the accelerator section, although in usual shock tube flow it attains some limit value when the shock has traveled sufficient distance and then leakage from the boundary layer at the contact surface balances the storage effect at the shock front. No gasdynamical shock attenuation was observed in the accelerator section.

Since the reproducibility of this type of shock tubes is not very good as is well known, the shock Mach numbers varied between about 16 and 18 for $p_1=2$ mmHg and between about 18 and 20 for $p_1=1$ mmHg, even though the conditions at the high pressure section were kept as constant as possible. The actual shock Mach numbers measured at the entrance of the accelerator were used in the data processing. It might be considered that this shock velocity scatter was mainly related to the bursting condition of the diaphragm.

The electrical conductivity of the plasma obtained in our shock tube was measured before by the magnetic induction probe method devised by Lin and others[5], and was reported previously[6]. It was about 60 mho/cm for $p_1=2$ mmHg in the shock Mach number range used in this experiment. Also it was confirmed from the response of the magnentic induction probe used in this work that the axial distribution of the electrical conductivity was approximately a step function rising at the shock front in this shock Mach number range.

The observed contact surface was of course not a clear discontinuity but a contact zone with some width. It also had some irregularity and was even fairly oblique in some cases. This was supposed to be due to the remaining effect of the irregularity of the diaphragm bursting process. The measurement of the contact surface position, i. e. the calculation of the plasma slug length, has a direct influence on the calculation of the electrical current density during the data processing. To be precise, the records showing too much irregularities were discarded, and the visually estimated centers of the contact zones were adopted as the contact surface positions to be used in the calculations.

3. 2. Acceleration experiments

The acceleration experiments were performed for several combinations of magnetic and electric field strength. For the experiments we had to synchronize the magnetic and electric field application with the arrival of the shock wave at the entrance of the accelerator. This was achieved by the combination of the delay circuit and the ignitron driver circuit as explained before. Photo 3 shows a simultaneous record of the magnetic field, the electrical current and the inter-electrode potential for a typical test run. It shows that the synchronization was satisfactory. The middle trace of this record shows the inter-electrode potential. Its initial step corresponds to the $u \cdot B$ voltage induced by the plasma flow and magnetic field between the electrodes before the shock front reaches the electric discharge trigger point. The next rise corresponds to the initiation of the electric current discharge and this second step shows the potential difference produced by the discharge current added to the initial $u \cdot B$ voltage.

We evaluated the records as above and those obtained when only the magnetic field was applied and the electrode circuit was opened. The quantitative tendency was similar to those of Hogan and Leonard. This seems to show that there existed no short-circuit path as might strongly hinder the plasma acceleration.

About 120 consecutive pictures were obtained during each experimental run, from which about 40–60 frames were selected to be processed by least square fitting to determine the instantaneous shock velocity.

While the high-speed photography, though more accurate, requires laborious processing to give necessary results, the streak camera is sometimes very convenient to make rough checks of the acceleration behavior, as it gives a direct record of the shock trajectory and even particle paths in some cases. However, its resolution is not satisfactory and the graphical differentiation necessary for a quantitative processing is very difficult. Moreover, it gives only the record of the flow seen through the slit at the tube axis. We tried to utilize those merits of the two systems as best as we could according to the cases.

A typical result of the ultra-high-speed photography is shown in Photo 5, where the change of the plasma configuration during the acceleration process is shown from top to bottom.

Though the shock front is nearly plane during the initial phase of the acceleration, it gradually changes shape and two spike shaped protrusions continue to grow near the upper and the lower electrodes. The amount of protrusion is comparatively larger at the positive electrode. This tendency of shock front deformation seems to be proportional to the $j \times B$ force and for a given amount of the $j \times B$ force, it is stronger for smaller p_1 (i. e. for $p_1 = 1$ mmHg), which seems to show that it is related to the relative strength of the force field.

Since the cross section of our accelerator was circular instead of being rectangular as required for an exact two-dimensional field application, we calculated the current density distribution by Fishmann's[7] method. The result showed the existence of current density concentration near the arc shaped electrodes. It may be considered that the strong interaction of this concentrated current with the magnetic field is the main cause of the shock front protrusion near the electrodes. We have not yet been able to explain the occurence of stronger protrusion near the positive electrode than near the negative one.

The deformation of the shock front continues to grow during the acceleration process, and almost covers the whole shock front near the exit of the accelerator, when the accelerative force field is considerably strong. Even after the exit from the accelerator, it shows only slight tendency to become flat.

Hogan also found the existence of such shock deformation when he observed the flow field with a streak camera from a vertical slit placed downstream of the accelerator. But he reported no observation about the growth of this phenomenon. We could obtain a fuller picture of its growth during the acceleration process, though the theoretical explanation is not yet sufficient.

A preliminary investigation of the shock behavior under an inverse $j \times B$ force was also performed. The shock front was of course decelerated in this case, and, instead of protruding, it was observed to be decelerated more in the neighborhood of the electrodes, hence showing a rounded shape. This may also show that the $j \times B$ force is stronger near the electrodes.

If the influence of these deformation tendencies should be considerably strong, it might invalidate the quasi-one-dimensional treatment. Although we used this assumption in the processing of the experimental data taking the more or less planer shock front near the tube axis as the typical shock position, more exact three-dimensional treatment might be necessary if much stronger $j \times B$ field should be used.

When the plasma slug is leaving the accelerator section, the electric current is concentrated to small areas around the edges of the electrodes and heats the boundary layer. This heating process produces trails of hot boundary layers which electrically connect the electrodes with the main plasma slug, and the residual electric charge in the capacitor bank continues to discharge through these layers which are kept at high temperature. This state is shown in the lower pictures of Photo 5, where the hot boundary layer trails are observed at the upper and the lower sides of the tube, while the central part is filled with the cold gas behind the contact surface. Hogan also found during the observation of the shock deformation that luminous layer remained near the tube wall long after the shock passage. Though there is no discussion about its mechanism in his report, this seems to correspond to the above phenomenon.

Although this phenomenon does not influence the behavior of the shock-heated flow inside the accelerator, it would naturally affect the inter-electrode potential after the plasma slug has left the accelerator.

It seems that Hogan used this behavior of the inter-electrode potential, i. e. the current vs. voltage characteristics, to estimate the equivalent resistance of the mixing region behind the contact surface. However, his report lacks details of the procedure, and, in addition, the shock-heated region had reached the limiting condition in his experiment, that is, the inflow at the shock front had been balanced by the leakage mass flow from the boundary layer at the contact surface, with no more plasma length increase, which was in contrast to the flow condition in our experiment.

If the mixing region has a certain amount of electrical conductivity, it works as a resistance connected in parallel with the plasma slug, and some portion of the total current flows through it. According to Hogan's treatments, the estimate of the equivalent resistance of the mixing region seems to have fairly strong influence on the overall momentum balance in the accelerator. Although we can only guess about the detail of his estimating procedure, the phenomenon described above might possibly have some influence on it.

So we tried to experimentally estimate the electrical conductivity of the mixing region more directly. As the inter-electrode potential was of the order of 100 to 200 volts when the current was discharged into the plasma in the acceleration experiments, about this amount of voltage was applied by a dry battery between a pair of narrow electrodes separately placed inside the accelerator, and the electrical current between these electrodes was observed while the shock-heated plasma traveled through the accelerator without the main current discharge.

This observation showed that the mixing zone was fairly narrow and that no electric current flowed through the non-luminous gas behind the mixing zone at this voltage level, which showed that whole of the supplied electric current could be considered to flow through the plasma slug during the acceleration process.

Photo. 4 shows a photograph taken by the streak camera, where the evidence of the acceleration of the shock-heated region can be seen. The maximum shock velocity increase which was obtained while the shock traveled through the accelerator was about 50 % for $p_1=2$ mmHg and 60 % for $p_1=1$ mmHg.

If the electric field circuit is opened and only the magnetic field of, for example, about 8,500 Gauss is applied, it might be expected that, when the plasma moves near the ends of the magnetic coils where the magnetic field intensity changes rapidly, the resulting eddy current might work as a loss mechanism. However, no shock front deceleration or deformation due to this effect was observed. On the other hand, when the electrodes were short-circuited in this configuration, fairly strong shock front deceleration due to the resulting inverse $j\times B$ force was observed.

4. Theoretical Considerations

In the theoretical considerations, the flow was treated as quasi-one-dimensional based on a physical model as shown in Fig. 1, and the experimentally observed three-dimensional phenomena such as the shock front protrusions were neglected.

It is not appropriate to apply the ideal gas relationship to the calculations of the shock transition when dealing with the plasma induced by a considerably strong shock. Thus the Rankine-Hugoniot relations including single-ionization was introduced into the shock front boundary condition, and the state of

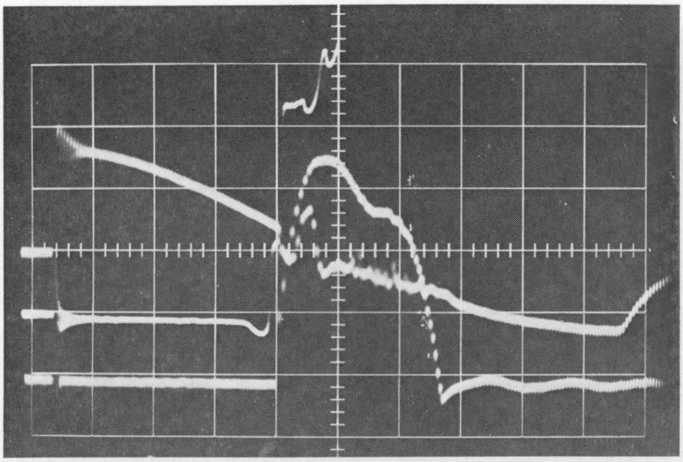

Photo 3 Record of measured electrical parameters for a typical run (100 μ sec/div., P_1=2 mm Hg, M_{so}=16.7, I_{max}=23,000 A., B=6,500 G)

Top ; Signal of the search coil for magnetic flux measurement.

Middle ; Potential difference between the electrodes. (Note the initial step indicating the induced $u \cdot B$ voltage.)

Bottom ; Current.

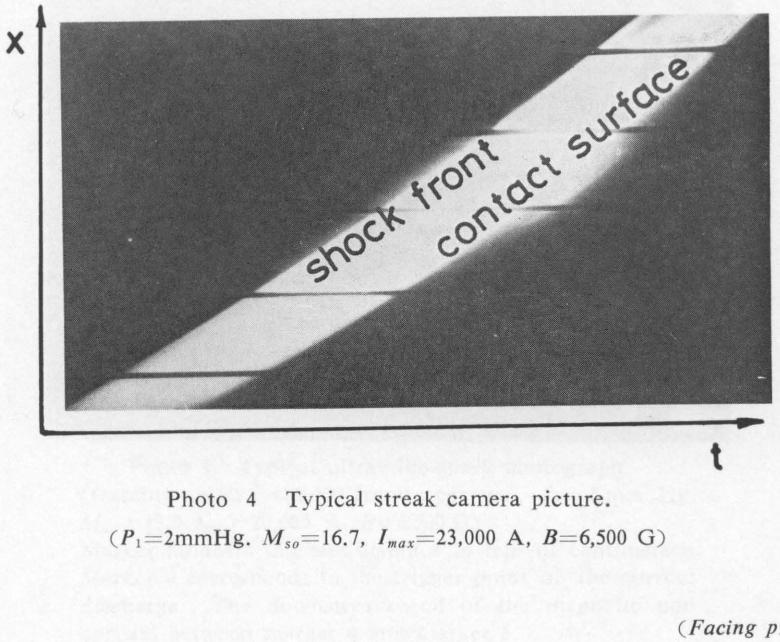

Photo 4 Typical streak camera picture.

(P_1=2mmHg. M_{so}=16.7, I_{max}=23,000 A, B=6,500 G)

(*Facing p.* 246)

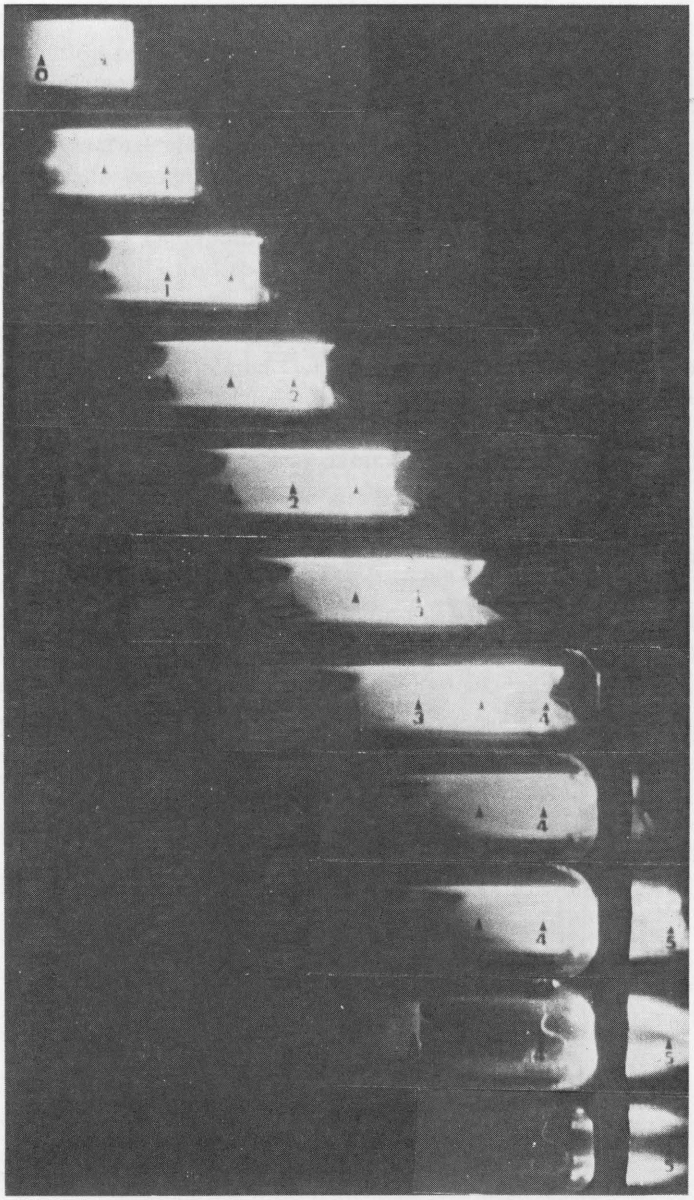

Photo 5 Typical ultra-high-speed photograph.
(framing speed $=482{,}000$ frames per sec., $P_1 = 2$ mm Hg, $M_{so} = 17.0$ $I_{max} = 20{,}000$ A, $B = 6{,}500$ G)
Marker numbers indicate distance in tens of centimeters. Marker 0 corresponds to the trigger point of the current discharge. The downstream end of the magnetic coil appears between marker 4 and marker 5.

the gas was assumed to attain equilibrium immediately behind the shock front without relaxation.

The contribution to the shock acceleration comes mainly from the $j\times B$ body force and the compressibility effect due to Joule heating. Since the amount of total current, and hence the corresponding current density j, is mainly determined by the external electrical source, the strength of the $j\times B$ body force may be considered to be determined externally without considerably depending on the value of the plasma electrical conductivity. This will be explained in more details later. The Joule heating effect, however, is closely related to the electrical conductivity and the way of state variations of the plasma.

Mainly to estimate the influence of this Joule heating effect, two different flow models were adopted. In one of them local equilibrium was assumed throughout the shock-heated region, while in the other the degree of ionization was assumed constant along the particle path irrespective of the state of the plasma. The latter model is called the frozen model in this paper. In both models the electrical conductivity was assumed to be constant. It may be expected that the former model gives a smaller estimate of the Joule heating effect, while the latter gives the largest limit. Mathematical expressions will be given for the equilibrium case in the following. The corresponding frozen equations can be easily derived as a special case.

The theoretical calculations were performed using the method of characteristics. The detailed derivation of these characteristic equations, and the characteristic equations for the frozen flow are given in Appendix A 1.

The characteristic equations are as follows.

$$\frac{\partial U}{\partial \alpha}+\frac{A}{(\gamma_{eff}-1)\cdot M_0\cdot G}\cdot\frac{\partial G}{\partial \alpha}=\frac{A}{(\gamma_{eff}-1)\cdot \overline{C}_{peff}\cdot M_0}\cdot\frac{\partial \overline{S}}{\partial \alpha}+\frac{I_L\cdot J}{\varphi}\left[\frac{\gamma_{eff}(1+\alpha_I)M_0\cdot J}{A\cdot \overline{C}_{peff}}+1\right]\left(\frac{d\tau}{d\alpha}\right) \tag{1}$$

along C^+characteristic (β=const.),

$$\frac{\partial U}{\partial \beta}-\frac{A}{(\gamma_{eff}-1)M_0\cdot G}\cdot\frac{\partial G}{\partial \beta}=-\frac{A}{(\gamma_{eff}-1)\overline{C}_{peff}\cdot M_0}\cdot\frac{\partial \overline{S}}{\partial \beta}-\frac{I_L\cdot J}{\varphi}\left[\frac{\gamma_{eff}(1+\alpha_I)M_0 J}{A\cdot \overline{C}_{peff}}-1\right]\left(\frac{d\tau}{d\beta}\right) \tag{2}$$

along C^- characteristic (α=const.)

And the energy equation is as follows.

$$\left(\frac{\partial \overline{S}}{\partial \alpha}\right)\cdot\left(\frac{d\tau}{d\beta}\right)+\left(\frac{\partial \overline{S}}{\partial \beta}\right)\cdot\left(\frac{d\tau}{d\alpha}\right)=\frac{2\gamma_{eff}(1+\alpha_I)\cdot M_0{}^2\cdot I_L\cdot J^2}{\varphi\cdot A^2}\cdot\left(\frac{d\tau}{d\alpha}\right)\cdot\left(\frac{d\tau}{d\beta}\right) \tag{3}$$

The characteristic directions are

$$\frac{dX}{d\alpha}=\left(U+\frac{A}{M_0}\right)\cdot\frac{d\tau}{d\alpha} \tag{4}$$

for C^+ characteristic,

$$\frac{dX}{d\beta}=\left(U-\frac{A}{M_0}\right)\cdot\frac{d\tau}{d\beta} \tag{5}$$

for C^- characteristic

Boundary conditions at the contact surface are

$$\frac{dX}{d\tau}=U, \tag{6}$$

$$dU\mp\left(\frac{\gamma_{eff}}{\gamma_3}\right)\cdot\frac{A_3}{\gamma_{eff}-1}\left(\frac{dG}{G}-\frac{d\bar{S}}{C_{peff}}\right)=0, \tag{7}$$

where suffix 3 shows the variable behind the contact surface. The second of the above conditions will be derived in Appendix A 2.

At the shock front, the boundary condition

$$\frac{dX}{d\tau}=\overline{U}_s, \tag{8}$$

is used together with the equilibrium Rankine-Hugoniot relations including single-ionization, which will be explained in Appendix A 2.

Some expressions for thermodynamic variables are

$$\gamma_{eff}=\left(\frac{C_p}{C_v}\right)\cdot\frac{1}{1-\dfrac{p}{1+\alpha_I}\left(\dfrac{\partial\alpha_I}{\partial p}\right)_T}\quad, \tag{9}$$

$$C_{peff}=\frac{C_p}{1+\dfrac{T}{1+\alpha_I}\left(\dfrac{\partial\alpha_I}{\partial T}\right)_p}\quad\text{(specially defined here.)}, \tag{10}$$

$$C_p=\left[\frac{5}{2}(1+\alpha_I)+\frac{\alpha_I}{2}(1-\alpha_I^2)\cdot\left(\frac{5}{2}+\frac{\Theta}{T}\right)^2\right]\cdot R \tag{11}$$

$$C_v=\left[\frac{3}{2}(1+\alpha_I)+\frac{\alpha_I(1-\alpha_I)}{2-\alpha_I}\left(\frac{3}{2}+\frac{\Theta}{T}\right)^2\right]\cdot R\quad, \tag{12}$$

The notation for several important variables are as follows.

U_S: shock velocity
u: particle velocity
a: velocity of sound
p: pressure
ρ: density
T: temperature
j: current density
B: magnetic flux density
E: the electric field intensity
σ: electrical conductivity

S : entropy

x : distance along tube axis

t : time

L : initial length of plasma slug

$g=p/\rho$: quantity specially defined here

C_p: specific heat at constant pressure

C_v: specific heat at constant volume

γ : specific heat ratio

R: gas constant

α_I: degree of ionization

I: total current

Also the following nondimensional parameters are defined. Suffix o indicates the initial state of plasma slug before the entrance into the accelerator.

$$U=u/u_0, \quad A=a/a_0, \quad \varphi=\rho/\rho_0, \quad \overline{S}=S/R,$$

$$X=x/L, \quad \tau=u_0t/L, \quad G=g/g_0, \quad \overline{C}_{peff}=C_{peff}/R,$$

$$J=j/\sigma u_0 B, \quad I_L=\sigma B^2 L/\rho_0 u_0, \quad \overline{U}_s=U_s/u_0,$$

$M_0=u_0/a_0$; initial Mach number of plasma.

The frozen flow corresponds to the case when $(\partial\alpha_I/\partial T)_p$, $(\partial\alpha_I/\partial p)_T=0$ in the above equations, hence for constant C_p and γ.

After the above equations are transformed into finite-difference forms, they are calculated along the charctaeristic net shown in Fig. 3, starting from the

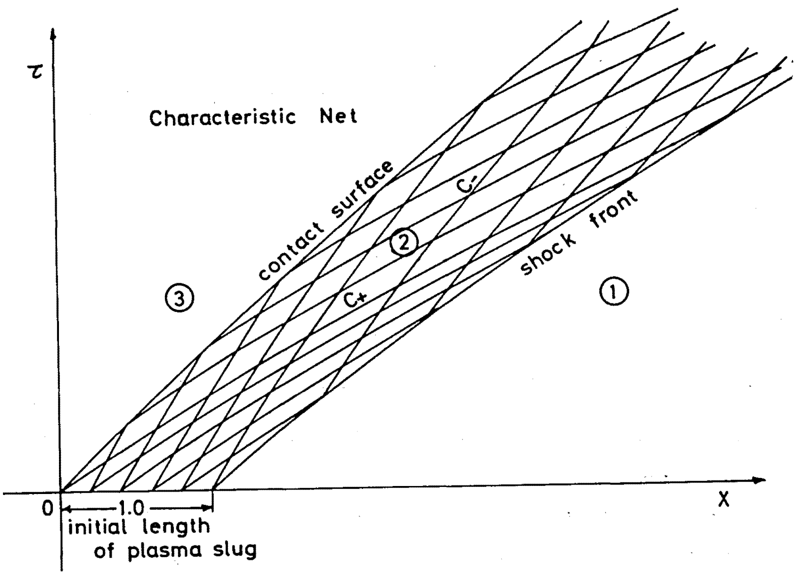

Fig. 3 An example of the characteristic net.

initial condition given on the X-axis at $\tau=\tau_0$. The boundary conditions are applied both on the contact surface and on the shock front. By repeating this step-by-step calculations, the shock velocity increase and the distributions of physical quantities for any instant of time can be calculated.

The current density j is given from the Ohm's law as

$$j=\sigma(E-u\cdot B). \tag{13}$$

Now we put the channel width as d, slug length as l, and the total current as I. Also E=constant as the electrode surfaces can be considered as equipotential surfaces, and the applied magnetic field B is constant. Since the amount of the total current, i. e. the integral of the above equation, is determined by the external conditions if the electrical conductivity distribution is assumed to be uniform, we get

$$E=\frac{I}{\sigma\cdot A_{slug}}+\frac{B}{l}\int_0^l u\cdot dx, \tag{14}$$

where $A_{slug}=l\cdot d$.

Substituting this into Eq. (13), we get

$$j=I/A_{slug}-\sigma(u-\bar{u})\cdot B=j_{app}-j_{ind}, \tag{15}$$

where

$$\bar{u}=\frac{1}{l}\int_0^l u\cdot dx\ ,\ j_{app}=I/A_{slug}\ ,\ j_{ind}=\sigma\cdot(u-\bar{u})\cdot B,$$

and $\bar{u}$ is the average slug velocity.

In other words the current density is given by the difference between j_{app} which is the total current devided by the cross-sectional area and j_{ind} which is caused by the induced potential. As j_{ind} is proportional to the local velocity deviation, the current density, and hence the resulting $j\times B$ force, is greater where the local velocity is smaller than the average slug velocity, and vice versa. Thus it acts to smooth out the velocity distribution, and vanishes when the whole plasma slug is uniformly accelerated.

However, it is impossible to introduce this term directly into the characteristic equations, since the calculation proceeds step-by-step along the characteristic net and it is difficult to obtain the integral of the velocity distribution at an arbitrary instant of time. So we performed the characteristic calculations neglecting it.

The calculated velocity distributions along the length of the plasma slug shown in Fig. 4 in the form of $\Delta u/u_0$ are fairly uniform. Since the effect of the j_{ind} term is to make the distribution still more uniform, it shows that there would be no important change in the velocity distribution if this term is neglected.

Fig. 5 shows an example of the calculated increase of the shock velocity with time τ for equilibrium and frozen models. Here the parameter F corresponding to the Lorentz body force is defined as $F=I_L\cdot J$. The shock velocity

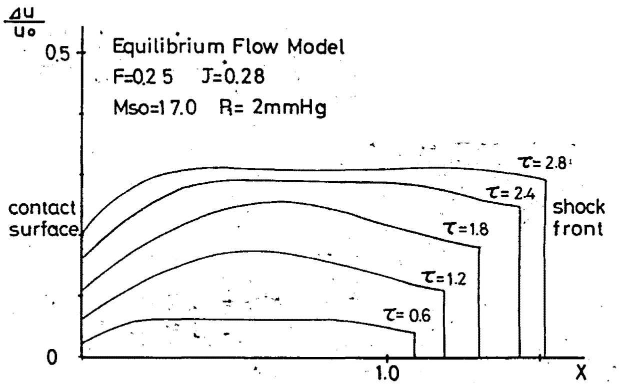

Fig. 4 Typical result of the velocity distribution change with time for the equilibrium model ($\Delta u = u - u_0$).

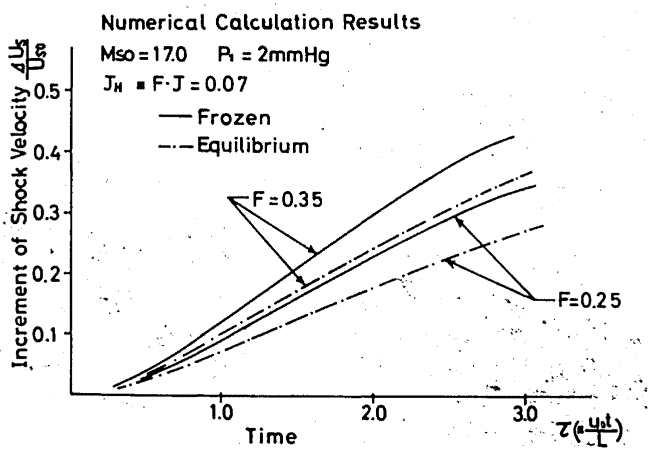

Fig. 5 Theoretical increment of the shock velocity with time τ ($\Delta U_s = U_s - U_{so}$).

increase is larger for the frozen model, perhaps because the Joule heating contributes to the acceleration in this case, while part of its energy is consumed in the ionization process in the equilibrium model. The difference between the two models is most pronounced for temperature distribution, which are shown in Fig. 6 (a) and Fig. 6 (b). The examples of the variation of pressure distribution with time are shown in Fig. 7 (a) and Fig. 7 (b) for the frozen and equilibrium model respectively. Another quantities ρ, etc. are also calculated but are not shown in the figures.

They show that the pressure begins to decrease near the contact surface after the initiation of acceleration and that this decrease is gradually propagated toward the shock front. After the C^+characteristic line starting from the point o in Fig. 3 has reached the shock front, these disturbances begin to influence

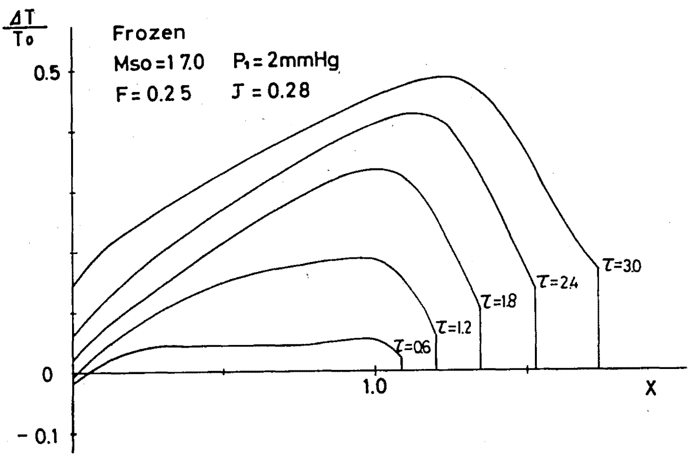

(a) for the frozen model.

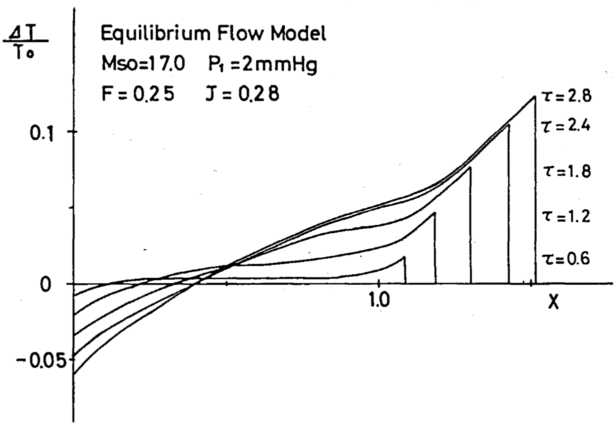

(b) for the equilibrium model.

Fig. 6 Typical result of the temperature distribution change with time ($\Delta T = T - T_0$).

the shock front behavior and decreases the amount of shock acceleration. However, the shock has traveled a certain distance before the initiation of this effect. According to the calculated result, this distance, though more or less changes according to the experimental conditions, is comparable to the accelerator length. In such a case, it will be theoretically permissible to apply the Rosciszewski rule to the acceleration process.

The Rosciszewski rule in the ideal gas case can be written as follows.

$$dr_w - \frac{a_w}{2\gamma} \cdot d\overline{S}_w = F_{\alpha w} \cdot dt_w \tag{16}$$

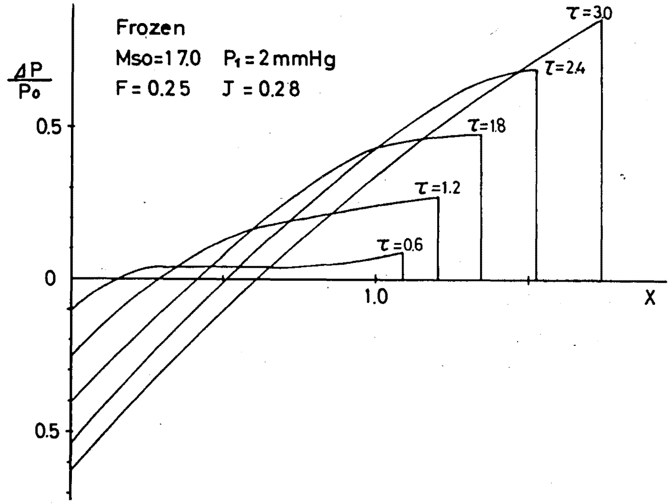

(a) for the frozen model.

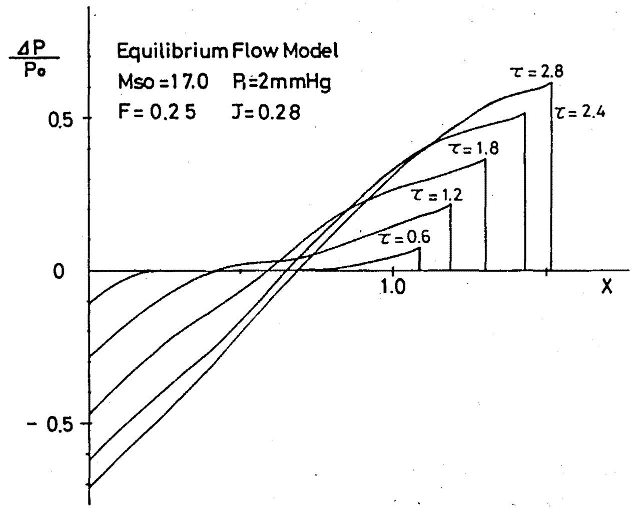

(b) for the equilibrium model.

Fig. 7 Typical result of the pressure distribution change with time ($\Delta p = p - p_0$).

where

$$r = \frac{u}{2} + \frac{a}{\gamma - 1}, \qquad F_\alpha = \frac{(\gamma-1)a}{2\gamma R} \cdot \frac{DS}{Dt} + \frac{j \cdot B}{2\rho}.$$

Suffix w denotes quantities at the shock front.

For the equilibirum flow, this can be transformed into the following equation showing the shock velocity variation with time.

$$\frac{d(\Delta M_s)}{d\tau}=\frac{I_L\cdot J\cdot(\rho_{210}-1)\cdot\left[\dfrac{(\rho_{210}-1)\cdot M_{so}\cdot J}{\rho_{210}\cdot C_{peff}}\left\{\dfrac{\gamma_1\cdot\gamma_{eff}(1+\alpha_I)}{T_{21}}\right\}^{1/2}+1\right]}{\left[\rho_{21}-1+\left[\dfrac{M_s}{\rho_{21}}+\left\{\dfrac{(1+\alpha_I)T_{21}}{\gamma_1\cdot\gamma_{eff}}\right\}^{1/2}\right]\left(\dfrac{d\rho_{21}}{dM_s}\right)+\rho_{21}\left(\dfrac{1}{\gamma_1\gamma_{eff}(1+\alpha_I)\cdot T_{21}}\right)^{1/2}\cdot\left\{(1+\alpha_I)\dfrac{dT_{21}}{dM_s}+T_{21}\dfrac{d\alpha_I}{dM_s}\right\}\right]}\,, \tag{17}$$

where

M_s: shock Mach number, $\rho_{21}=\rho_2/\rho_1$, $T_{21}=T_2/T_1$,

$$\Delta M_s=\frac{M_s-M_{so}}{M_{so}}\doteq\frac{\Delta U_s}{U_{so}}.$$

Suffix 1 indicates quantities in front of the shock, while suffix 2 indicates those in the shock-heated region. The frozen equation can be similarly obtained by taking C_p and γ to be constant.

Certain terms are neglected as the second order quantities in deriving this rule. The validity of this assumption in the range of shock acceleration considered in our experiments can only be verified through comparison with the more exact characteristic step-by-step calculations. The result of the comparison is shown in Fig. 8, where the meaning of the abscissa ξ will be explained in the next section. As shown here, the difference between the two calcluation are small, and it seems to be possible to use the Rosciszewski rule in the evaluation of the experimental results.

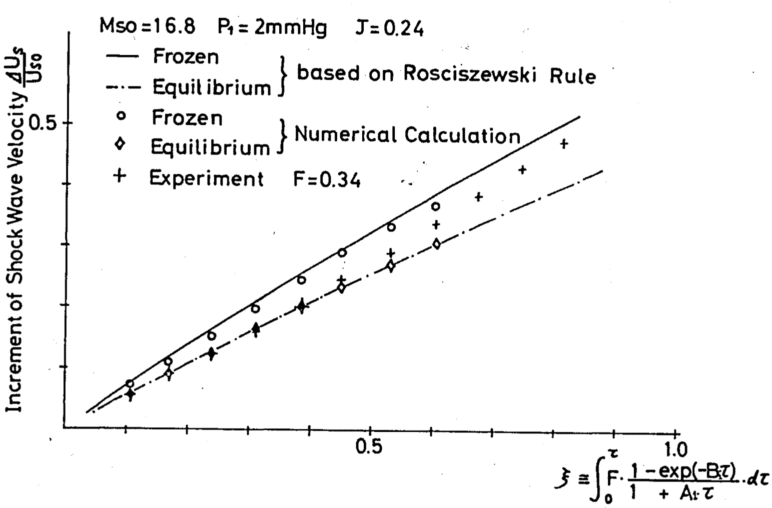

Fig. 8 Comparison of the results of the step-by-step calculation with that based on the Rosciszewski rule.

As explained before, the shock acceleration may theoretically decrease even while the plamsa is inside the accelerator, if the disturbances generated in the neighborhood of the contact surface begin to propagate to the shock front, as shown by the result of the step-by-step calculations. When the plasma slug has left the accelerative field and the $j \times B$ force ceased to accelerate it, for example, the shock wave can be expected to show more or less deceleration caused by the readjustment from the electro-magnetically balanced state to the gasdynamically balanced state.

The above process might be confirmed by the step-by-step calculations, if we could continue it after introducing the condition that the $j \times B$ force vanishes at the exit of the accelerator. Actually this is very difficult however, because the degradation of the convergence and the accuracy caused mainly by the strong irregularity of the characterisic net at some points or the accumulated round-off errors becomes so grave as to destroy the whole calculation, if we should simply try to continue the calculation for sufficient steps. We tried to overcome this difficulty by recording the calculated result at some instant of time and, after rearranging the characteristic net with uniform spacing, resuming the calculation from this new initial condition. We have not succeeded with this scheme yet, due to some difficulties in accurately interpolating the calculated results to obtain the new initial condition.

Also the experimental behavior of the flow after leaving the accelerator has not been clarified yet, because the shock deformation makes accurate observations quite difficult and we can not understand how the heating of the driver gas near the wall due to the residual electrical discharge should effect on the plasma main flow.

5. Discussions

As explained before, the reproducibility of the combustion shock tube is not very good. This, together with the fact that the electric and magnetic field strength did not exactly attain the planned values, makes the comparison of the experimental and the theoretical results rather difficult. The experimental condition differs slightly for each test run, and, if a really exact comparison should be required, the characteristic step-by-step calculation would have to be performed for individual test condition.

Thus in Fig. 9 a typical experimental result is compared with the calculated result based on the experimental values of M_{so}, F, J, etc. This experimental result seems to fall closer to the equilibrium result. Though this is the general tendency, not all of the experimental results show such clear tendency.

Since it is difficult to evaluate all test data in such a way and even more difficult to repeat the lengthy characteristic calculations for all test conditions, it seems to be more convenient to evaluate them using the Rosciszewski rule, for example, Eq. (17).

In the comparison with the theoretical result, it would be ideal if the cur-

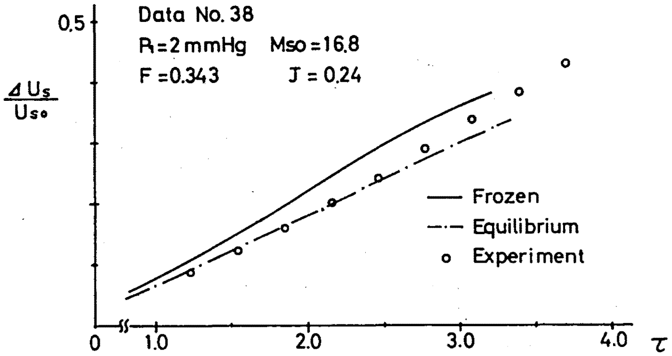

Fig. 9 Direct comparison of the step-by-step calculation results of shock velocity increment with a typical experimental result.

rent wave form for the electric field application were a step function. But the actual one is a function of time as shown in Photo 1. The influence of this actual current wave form and the current density decrease caused by the fact that the slug length gradually increases in the accelerator, was represented in a function form, which correponds to the terms inside the parentheses in the integrand of Eq. (18). The current denstiy was assumed to be constant along the tube axis and was calculated from the slug length and the channel width which was taken equal to the length of one side of a square having the same cross-sectional area as the actual circular accelerator.

Eq. (17) can be explicitly integrated by the separation of variables if the first term of the bracket in the numerator of the right hand side, which is related to the Joule heating, may be assumed to be constant with time. As the result, the following parameter appears as an independent variable,

$$\xi=\int_0^{\tau} F\cdot\left\{\frac{1-exp(-B_1\cdot\tau)}{1+A_1\cdot\tau}\right\}\cdot d\tau, \tag{18}$$

where

$F=I_L\cdot J$

A_1, B_1 : Experimental constants.

The shock velocity increase can be evaluated in terms of this parameter ξ, which may be called the interaction time. The results of this calculations are shown in Fig. 8. Fig. 10 (a) and Fig. 10 (b) show the experimental results for $p_1=2$ mmHg and $p_1=1$ mmHg respectively. The experimental points are marked with various symbols in terms of nominal values of J which corresponds to the amount of Joule heating. No regular dependency on J can be found from this figure.

To examine this point more closely, another approach to the data evaluation was attempted. If we examine the results of the step-by-step calculations

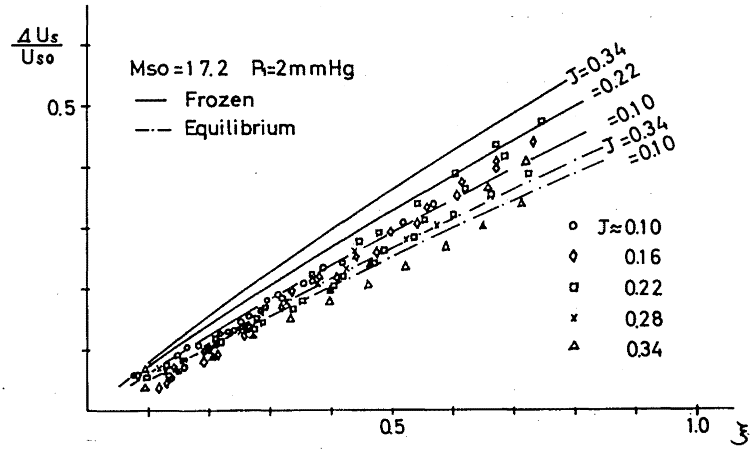

(a) for P_1=2 mmHg at M_{SO}=17.2

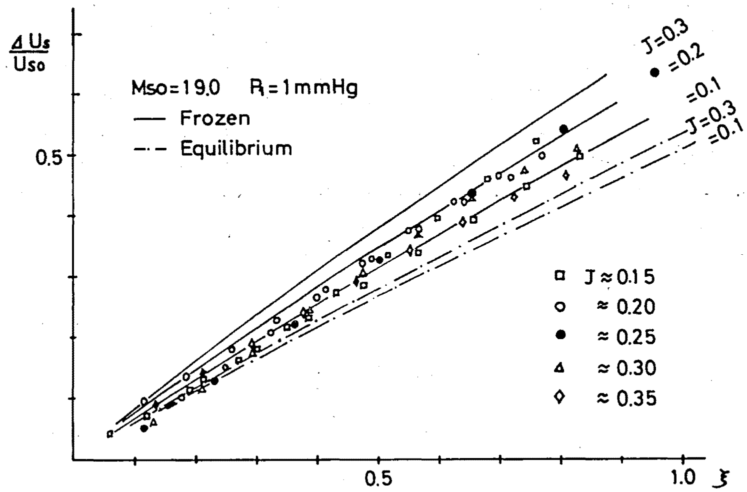

(b) for P_1=1 mmHg at M_{SO}=19.0

Fig. 10 Comparison of the experimental results with theoretical results based on Rosciszewski rule. ξ is difined in Eq. (18).

closely, we can see that the amount of shock velocity increase at some instant of time depends more or less linearly on F, if $J_H(\equiv j^2 \cdot L/\sigma \rho_0 u_0^3)$, which represents the Joule heating term, is kept constant. This relationship is shown in Fig. 11 (a). For the frozen case, $\Delta U_s/U_{so}$ is about 10% when F approaches zero for τ=2.8, which roughly corresponds to the end of the acceleration phase. This corresponds to the case where only the magnetic field B is made to approach zero. When the same limitting process is applied to the equilibrium result,

$\Delta U_s/U_{so}$ seems to approach zero without any clear dependence on τ.

Since the experimental values of J_H scatter widely, it is difficult to apply this approach to them directly. As one attempt, the experimental results of shock velocity increase for $\tau=3.0$ were plotted against F in Fig. 11 (b), without any attempt to classify them in terms of J_H. Most of the data points seem to fall around a straight line which seems to converge to zero with decreasing value of F. The data points might scatter more widely if they depended on J_H.

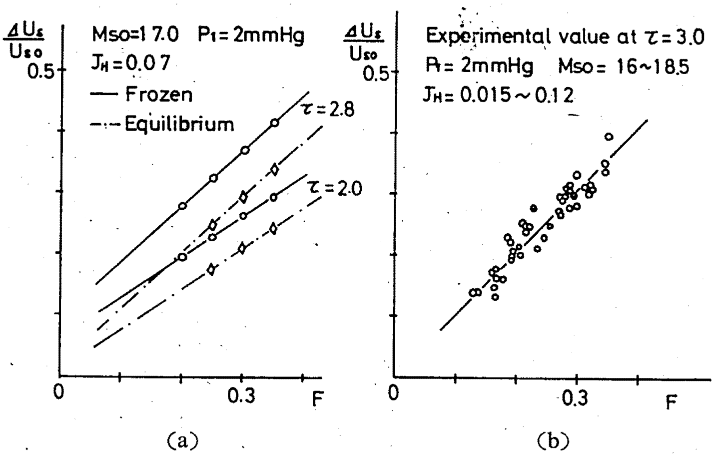

Fig. 11 (a) Theoretical dependence of the shock velocity increment on F.
(b) Dependence of various experimental points on F.

Although the above discussions are incomplete, they seem to suggest that the Joule heating effect does not contribute to the shock acceleration very much and that this might be explained if the variation of state in the shock-heated region can be assumed to be in local equilibrium. Also, no evidence of acceleration was observed experimentally, when only the electric current of about $j=400$ A/cm^2 was applied. This is in contrast to Hogan's report that a certain amount of acceleration existed with only the electric field. Though it can be considered that this may be due to the effect of backstrapping, we are unable to give fuller explanation of the difference at present.

As shown in Fig. 9 and Fig. 10, the experimental data of the shock acceleration tend to increase toward the end of the acceleration process in contrast to the theoretical expectations. This may be partly due to the inaccuracy of the least square fitting method used to calculate the shock velocity. Another important reason might be the inaccuracy of the assumption that the current density is constant along the tube axis. As the shock strength increases during the acceleration, the electrical conductivity might be increased near the shock front while it might be decreased near the contact surface by rarefaction effects. It is possible that there should exist a nonuniform current distribution due to these effects which may increase the local interactive force near the shock front.

Though we have neglected all loss mechanisms during the above treatments, the experimental results seem to be in reasonable agreement with the theoretical results. Although more detailed investigations are undoubtedly necessary, this might suggest that no significant loss mechanism appears in the acceleration process of our experiment.

6. Conclusions

(1) The behavior of the shock front and the plasma slug, and the amount of increase in shock front velocity during the $j\times B$ acceleration were observed with a 500,000 frames/sec ultra-high-speed camera.

(2) The deformation of the shock front during the acceleration was observed.

(3) Calculations by the method of characteristics were performed assuming the shock-heated plasma to be either in equilibrium or frozen, and the distributions of temperature, particle velocity, the increment of the shock velocity, etc. under the effect of $j\times B$ force were obtained.

(4) The experimental data of the shock velocity increase agree more closely with the results of the equilibrium calculations.

(5) The experimental data of shock velocity increase plotted against F fall rather close to a straight line.

(6) The effect of Joule heating on the acceleration of the shock wave was discussed.

Acknowledgements

The experimental part of this work was supported by the grant in aid for scientific research of the Ministry of Education.

We would like to express our profound gratitude to Mr. A. Sakurai, assistant of our department, for his devoted help in our experimental and theoretical investigations.

References

1) Hogan, W. T., Experiments with a Transient dc Cross-Field Accelerator at High Power Levels, in N. W. Mather and G.W., Sutton (eds.), *Proceedings of the 3rd Symposium on Engineering Aspects of magnetohydrodynamics*, Gordon and Breach, Science Publishers, Inc., New York, 1964, pp. 479–505.
2) Leonard, R. L. and Fay, J. A., Experiments on a Quasi-Steady $j\times B$ Accelerator, AIAA J. Vol. 3, No. 1, Jan. 1965, pp. 115–121.
3) Rosciszewski, J. and Oppenheim, A. K., Shock Interaction with an Electromagnetic Field, Physics of Fluids, Vol. 6, No. 5, May 1963, pp. 689–698.
4) Mirels, H. and Braun, W. H., Perturbed One-Dimensional Unsteady Flows Including Transverse Magnetic-Field Effect, Physics of Fluids, Vol. 5, No. 3, March 1962, pp. 259-265.

5) Lin, S. C., Resler, E. L. and Kantrowitz, A., Electrical Conductivity of Highly Ionized Argon Produced by Shock Waves, J. Appl. Phys., Vol. 26, 1955, pp. 95-105.
6) Shibata, K. and Iwasaki, M., Experiments on the Electrical Conductivity of Plasmas produced by a Combustion Driven Shock Tube, Technol. Rept. Kyushu Univ., Vol. 42, No. 3, 1969, (in Japanese), pp. 691-698.
7) Fishmann, F., Steady Magnetohyrodynamic Flow through a Channel of Circular Section, *Advanced Energy Conversion*, Pergamon Press, vol. 4, 1964, pp. 1-14.

(Received September 30, 1971)

Appendix

A 1. The Derivation of Characteristic Equations

Neglecting heat conductivity and viscosity and assuming the flow to be quasi-one-dimensional, the governing equations for our problem are given as follows:

Continuity
$$\frac{\partial \rho}{\partial t}+u\cdot\frac{\partial \rho}{\partial x}+\rho\cdot\frac{\partial u}{\partial x}=0, \qquad \text{(A 1)}$$

Momentum
$$\frac{\partial u}{\partial t}+u\cdot\frac{\partial u}{\partial x}+\frac{1}{\rho}\cdot\frac{\partial p}{\partial x}=f(x,\ t), \qquad \text{(A 2)}$$

Energy
$$\frac{\partial S}{\partial t}+u\cdot\frac{\partial S}{\partial x}=\frac{q(x,\ t)}{\rho\cdot T}, \qquad \text{(A 3)}$$

Equation of state
$$p=(1+\alpha_I)\cdot\rho RT, \qquad \text{(A 4)}$$

where function $f\ (x,\ t)$ reprerents the body force term and $q\ (x,\ t)$ the heat source term.

Notations for each variables are the same as in Section 4 unless specifically defined here.

Noting that the flow is non-isentropic, following characteristic equations can be easily obtained from Eq. A 1 and Eq. A 2 after some manipulations.

$$\left[\frac{\partial u}{\partial t}+(u\pm a)\frac{\partial u}{\partial x}\right]\pm\left(\frac{a}{\rho}\right)\left[\frac{\partial \rho}{\partial t}+(u\pm a)\frac{\partial \rho}{\partial x}\right]+\frac{1}{\rho}\cdot\left(\frac{\partial p}{\partial S}\right)_\rho\cdot\frac{\partial S}{\partial x}=f(x,\ t) \qquad \text{(A 5)}$$

On the other hand from the second law of thermodynamics,

$$T\cdot dS=C_v\cdot\left(\frac{\partial T}{\partial p}\right)_v\cdot dp+C_p\cdot\left(\frac{\partial T}{\partial v}\right)_p\cdot dv, \qquad \text{(A 6)}$$

where and v is the specific volume. Also from Eq. A 4,

$$\left(\frac{\partial T}{\partial v}\right)_p=\left(\frac{T}{v}\right)\cdot\frac{1}{1+\dfrac{T}{1+\alpha_I}\left(\dfrac{\partial \alpha_I}{\partial T}\right)_p} \qquad \text{(A 7)}$$

$$\left(\frac{\partial T}{\partial p}\right)_v=\left(\frac{T}{p}\right)\cdot\frac{1-\frac{p}{1+\alpha_I}\cdot\left(\frac{\partial\alpha_I}{\partial p}\right)_T}{1+\frac{T}{1+\alpha_I}\cdot\left(\frac{\partial\alpha_T}{\partial T}\right)_p}. \tag{A 8}$$

Putting those into Eq. A 6, we obtain

$$dS=\frac{C_{peff}}{\gamma_{eff}}\left(\frac{dp}{p}-\gamma_{eff}\frac{d\rho}{\rho}\right), \tag{A 9}$$

where

$$\gamma_{eff}=\frac{C_p}{C_v}\cdot\frac{1}{1-\frac{p}{1+\alpha_I}\left(\frac{\partial\alpha_I}{\partial p}\right)_T}$$

$$C_{peff}=\frac{C_p}{1+\frac{T}{1+\alpha_I}\cdot\left(\frac{\partial\alpha_I}{\partial T}\right)_p}$$

The specific heats of single-ionized monatomic gas are obtained from the expression for the enthalpy and the internal energy as

$$C_p=\left(\frac{\partial h}{\partial T}\right)_p=\left[\frac{5}{2}(1+\alpha_I)+\left(\frac{5}{2}T+\Theta\right)\cdot\left(\frac{\partial\alpha_I}{\partial T}\right)_p\right]\cdot R, \tag{A 10}$$

$$C_v=\left(\frac{\partial e}{\partial T}\right)_v=\left[\frac{3}{2}(1+\alpha_I)+\left(\frac{3}{2}T+\Theta\right)\cdot\left(\frac{\partial\alpha_I}{\partial T}\right)_v\right]\cdot R, \tag{A 11}$$

where h is the enthalpy and e is the internal energy and Θ is the characteristic temperature for ionization. If equilibrium state is assumed, Saha's equation can be used, which is given for single-ionized argon as

$$\alpha_I=\left[2.540\times10^5\times\frac{p}{T^{5/2}}\cdot exp\left(\frac{1.821\times10^5}{T}\right)+1\right]^{-1/2}. \tag{A 12}$$

Hence, we can obtain the following relations.

$$\left(\frac{\partial\alpha_I}{\partial p}\right)_T=\frac{-\alpha_I}{2p}(1-\alpha_I^2), \tag{A 13}$$

$$\left(\frac{\partial\alpha_I}{\partial T}\right)_p=\frac{\alpha_I}{2T}(1-\alpha_I^2)\cdot\left(\frac{5}{2}+\frac{\Theta}{T}\right). \tag{A 14}$$

Using these and Eq. A 8 from Eq. A 10 and Eq. A 11, we can obtain Eq. (11) and Eq. (12) in Section 4.

Now if we can assume the flow to be in equilibrium change, the $(\partial p/\partial S)_\rho$ term in Eq. A 5 can be written as follows using Eq. A 9;

$$\left(\frac{\partial p}{\partial S}\right)_\rho=\frac{\rho a^2}{C_{peff}}. \tag{A 15}$$

If we define a new variable g as

$$g=\frac{a^2}{\gamma_{eff}}=\frac{p}{\rho}, \tag{A 16}$$

and introduce it into Eq. A 9, we get

$$\left(\frac{a}{\rho}\right)\cdot d\rho=\frac{\gamma_{eff}}{(\gamma_{eff}-1)}\cdot\left(\frac{1}{a}\cdot dg-\frac{a}{C_{peff}}\cdot dS\right). \tag{A 17}$$

By putting Eq. A 15 and Eq. A 17 into Eq. A 5, and define the following differential operators in addition,

$$\frac{\partial}{\partial\alpha}\equiv\frac{\partial}{\partial t}+(u+a)\frac{\partial}{\partial x}, \qquad \frac{D}{Dt}\equiv\frac{\partial}{\partial t}+u\frac{\partial}{\partial x},$$

$$\frac{\partial}{\partial\beta}\equiv\frac{\partial}{\partial t}+(u-a)\frac{\partial}{\partial x},$$

we can obtain a pair of characteristic equations as

$$\frac{\partial u}{\partial\alpha}+\frac{\gamma_{eff}}{(\gamma_{eff}-1)a}\cdot\frac{\partial g}{\partial\alpha}=\frac{a}{(\gamma_{eff}-1)C_{peff}}\cdot\frac{\partial S}{\partial\alpha}+\frac{a}{C_{peff}}\cdot\frac{DS}{Dt}+f(x,\ t), \tag{A 18}$$

$$\frac{\partial u}{\partial\beta}-\frac{\gamma_{eff}}{(\gamma_{eff}-1)a}\cdot\frac{\partial g}{\partial\beta}=-\frac{a}{(\gamma_{eff}-1)C_{peff}}\cdot\frac{\partial S}{\partial\beta}-\frac{a}{C_{peff}}\cdot\frac{DS}{Dt}+f(x,\ t) \tag{A 19}$$

We have to introduce now the actual content of $f(x,t)$ and $q(x, t)$. The former is the $j\times B$ Lorentz force term and the latter is the Joule heating term, given respectively as

$$f(x,\ t)=\frac{j\cdot B}{\rho}, \qquad q(x,\ t)=\frac{j^2}{\sigma}. \tag{A 20}$$

Also DS/Dt is given from the energy equation Eq. A 3' and so Eq. A 18 and Eq. A 19 become Eq. (1) and Eq. (2) respectively when expressed with the nondimensional quantities defined in Section 4.

The characteristic equations for the frozen flow can be derived more simply. Since $(\partial\alpha_I/\partial T)_p=(\partial\alpha_I/\partial p)_T=0$, so C_p=const., C_v=const., γ=const. = 5/3 and $(\partial p/\partial S)_\rho=\rho a^2/C_p$.

Also the equation corresponding to Eq. A 17 becomes

$$\left(\frac{a}{\rho}\right)\cdot d\rho=\frac{2}{\gamma-1}\cdot da-\frac{\gamma\cdot a}{(\gamma-1)\cdot C_p}\cdot dS. \tag{A 21}$$

Using these and also defining

$$r=\frac{u}{2}+\frac{a}{\gamma-1},$$

(Riemann prameter)

$$s=\frac{u}{2}-\frac{a}{\gamma-1},$$

$$F_\alpha=\frac{(\gamma-1)}{2\gamma(1+\alpha_I)}\cdot\frac{DS}{Dt}+\frac{j\cdot B}{2\rho}\ ,$$

$$F_\beta=\frac{\gamma-1}{2\gamma(1+\alpha_I)}\cdot\frac{DS}{Dt}-\frac{j\cdot B}{2\rho}\ ,$$

The characteristic equations for this case are obtained as

$$\frac{\partial r}{\partial\alpha}=\frac{a}{2\gamma(1+\alpha_I)R}\cdot\frac{\partial S}{\partial\alpha}+F_\alpha\ , \tag{A 22}$$

$$\frac{\partial s}{\partial\beta}=\frac{a}{2\gamma(1+\alpha_I)R}\cdot\frac{\partial S}{\partial\beta}-F_\beta \tag{A 23}$$

Each of these systems of characteristic equations is transformed into finite-difference form and numerically calculated along the characteristic lines. The actual computation may be divided into three parts, i. e. the calculation at the shock front or the contact surface satisfying the boundary conditions, and the calculation of the system of characteristic equations at the internal points. The calculations at each net point are performed by an iteration process.

Especially for the equilibrium case, Saha's equation has to be solved after p and g are obtained, thus adding more iterative processes.

A 2. Boundary Conditions

The boundary condition at the contact surface will be given first. The notation used in the following explanations is shown in Fig. 3.

For the equilibrium case, we will consider the relations in differential form. Region (3) is isentropic, so following relation holds.

$$\frac{dp_3}{p_3}=\frac{2\gamma_3}{\gamma_3-1}\cdot\frac{da_3}{a_3}\ . \tag{A 24}$$

Also the Riemann invariant is conserved on each characteristic line emanating from a constant state in region (3). Hence following relation holds at the contact surface.

$$dU_3+\frac{2da_3}{\gamma_3-1}=0 \tag{A 25}$$

Also in region (2), Eq. A 17 holds at the contact surface. Combining these with the conditions

$$p_2=p_3,\qquad u_2=u_3,$$

we obtain Eq. (7) in Section 4 as the boundary condition.

For the frozen case, the corresponding boundary condition can be obtained in an integrated form as γ, C_p etc. are constant.

$$u-u_0=\frac{2a_{30}}{(\gamma_3-1)}\cdot\left[\left(\frac{a}{a_0}\right)^{\frac{\gamma(\gamma_3-1)}{\gamma_3(\gamma-1)}}\cdot exp\left\{\frac{-(\gamma_3-1)}{2\gamma_3(1+\alpha_I)R}(S-S_0)\right\}-1\right]. \qquad \text{(A 26)}$$

The shock front boundary conditions are obtained from the three conservation equations and the expression for the enthalpy

$$\rho_1 U_s=\rho_2(U_s-u_2), \qquad \text{(A 27)}$$

$$p_1+\rho_1 U_s^2=p_2+\rho_2(U_s-u_2)^2, \qquad \text{(A 28)}$$

$$h_1+\frac{U_s^2}{2}=h_2+\frac{1}{2}(U_s-u_2)^2, \qquad \text{(A 29)}$$

$$h_2=\left[\frac{5}{2}(1+\alpha_I)\,T_2+\alpha_I\cdot\Theta\right]\cdot R, \qquad \text{(A 30)}$$

together with the Saha's equation and equation of state, for the equilibrium transition of single-ionized monatomic gas.

Since, for example, the actual form of the Saha's equation is too complex to be solved analytically together with the above three conservation equations etc., usually solutions of these relations depend on lengthy numerical calculations.

This shows that it would be quite inefficient to repeat the calculation of the shock relations for the numerous calculational points at the shock front in each computational run. Hence in the actual computation, the shock relations for various initial conditions and shock Mach numbers were first calculated in a table form, and the shock front boundary conditions for each computational run were interpolated from this table. This procedure proved to be satisfactory both in accuracy and efficiency.

These computations were performed by FACOM 230-60 in the Computer Center, Kyushu University.